catalysts

MDPI

Article

Catalytic Combustion of Toluene over Highly Dispersed Cu-CeO_x Derived from Cu-Ce-MOF by EDTA Grafting Method

Wenjie Sun, Yijia Huang, Xiaomin Li, Zhen Huang, Hualong Xu and Wei Shen *

Collaborative Innovation Center of Chemistry for Energy Materials, Shanghai Key Laboratory of Molecular Catalysis and Innovative Materials and Laboratory of Advanced Materials, Department of Chemistry, Fudan University, Shanghai 200433, China; wjsun17@fudan.edu.cn (W.S.); yjhuang20@fudan.edu.cn (Y.H.); xmli17@fudan.edu.cn (X.L.); huangzhen@fudan.edu.cn (Z.H.); shuhl@fudan.edu.cn (H.X.)
* Correspondence: wshen@fudan.edu.cn

Abstract: In this work, Cu-CeO_x-MOF catalysts with well-dispersed Cu in different contents were synthesized via the ethylenediaminetetraacetic acid (EDTA) grafting method. EDTA was grafted in Ce-MOF-808 to anchor Cu and then the metal-organic frameworks (MOFs) were utilized as sacrificial template to form highly performed Cu-CeO_x-MOF for toluene catalytic combustion. In this series of samples, Cu-CeO_x-MOF-0.2 had a higher ratio of $O_\alpha/(O_\alpha+O_\beta)$, more oxygen vacancies and performed better low-temperature reducibility. Cu-CeO_x-MOF-0.2 showed outstanding catalytic activity and stability. The T_{90} (temperature when toluene conversion achieved 90%) of Cu-CeO_x-MOF-0.2 was 226 °C at 60,000 mL/(g_{cat}·h). In situ diffuse reflectance infrared transform spectroscopy (in situ DRIFTS) results revealed that the opening of aromatic ring and the deep oxidation of carboxylate were key steps for toluene catalytic combustion over Cu-CeO_x-MOF-0.2.

Keywords: metal-organic frameworks; catalytic combustion; volatile organic compounds; grafting method; ceria

Citation: Sun, W.; Huang, Y.; Li, X.; Huang, Z.; Xu, H.; Shen, W. Catalytic Combustion of Toluene over Highly Dispersed Cu-CeO_x Derived from Cu-Ce-MOF by EDTA Grafting Method. *Catalysts* **2021**, *11*, 519. https://doi.org/10.3390/catal11040519

Academic Editors: Simona M. Coman and Joanna Goscianska

Received: 31 March 2021
Accepted: 17 April 2021
Published: 20 April 2021

1. Introduction

Over recent years, the emission of volatile organic compounds (VOCs) has been viewed as a crucial environmental problem around the world [1,2]. VOCs are regarded as not only a spur to the increasingly serious air pollution, but the main hazardous substances to public health as well [3]. Toluene is a typical aromatic hydrocarbon in VOCs with representative structure and considerably huge emission [4], arousing a wide concern. Multiple technologies have been performed for toluene removal such as thermal combustion, physical and chemical adsorption [5], biological decomposition [6], plasma-assisted catalytic removal [7] and catalytic combustion. Catalytic combustion has been proven as an extensive and promising technique for toluene processing on account of the better destructive efficiency, lower operation temperature and less harmful byproducts, in which the key issue is the development of high-performance catalysts [8].

Numerous transition metal oxides are verified to be effective catalysts for toluene catalytic combustion. Cu-[9], Mn-[10], Co-[11] and Ce-[12] based oxides are widely researched due to their rich variety, low cost and long service life [13]. Toluene catalytic combustion process with transition metal oxide catalysts has been generally considered to follow the Mars-van Krevelen (MvK) mechanism [14,15]. Transition metal oxide catalysts provide oxygen species for toluene oxidation and subsequently, the consumed oxygen species are replenished by gas phase oxygen, achieving the catalytic reaction cycle. It is mainly accepted that highly active oxygen species were crucial for oxygen-involved oxidation-reduction reactions. CeO_2 has abundant oxygen vacancies, which could promote the adsorption and activation of oxygen in the reaction process. Thus, CeO_2 has been widely applied in VOCs catalytic combustion, automotive three-way catalysts, solid oxide fuel cells and so on [16]. However, the catalytic activity of CeO_2 still needs improvement.

Enhancement of specific surface area and introduction of additional metal component are two effective means to improve the catalytic activity of transition metal oxide catalysts [17,18]. For example, Cu could be used as the second component, and introduction of highly dispersed Cu could effectively improve the catalytic activity [19,20]. However, it is difficult to prepare highly uniform Cu on CeO_2 through common introduction methods, such as the wet impregnation method [21].

In our previous work, Ce-MOF-808 with three-dimensional porous structure was used as the precursor to prepare the CeO_2 catalyst. The prepared CeO_2-MOF-808 with large specific surface area and abundant active sites showed good catalytic performance [19,22]. The uniformity of metal–organic frameworks (MOFs) [23,24] provides the possibility for highly dispersed introduction of Cu [25]. It is worth mentioning that through the ligand exchange method, ligands with metal ions chelating capacity could be grafted onto MOF and then the second metal component could be introduced into MOF structures with atomic dispersion [26,27]. Therefore, the highly uniformly dispersed transition metal oxide catalyst could be obtained by calcination. Peng [28,29] et al. reported a post-synthetic modification treatment for incorporating ethylenediaminetetraacetic acid (EDTA) ligands on Zr-MOF-808 and the Zr-MOF-808-EDTA was applied as a heavy metal ion trap with high efficiencies. Nonetheless, the application of EDTA grafting method on Ce-MOF-808 for Cu introduction for toluene catalytic combustion has not been reported.

The investigation of intermediates is helpful to understand the reaction mechanism of toluene catalytic combustion. The pathway of toluene oxidation was reported to be different over diverse oxides. The adsorbed toluene was oxidized to form toluene, benzyl alcohol, benzaldehyde, benzoate, benzene, phenol, benzoquinone, maleic anhydride, CO_2 and H_2O on Co_3O_4 catalysts [30]. While on CeO_2 and Au/CeO_2 catalysts, the aromatic ring of toluene was first destabilized, resulting in a complete oxidation to CO_2 and H_2O [31]. As far as we know, the corresponding mechanism of toluene catalytic combustion over $CuCeO_x$ catalysts, as a significant issue, has not been further studied.

Herein, we developed Cu-CeO_x-MOF-n catalysts with well-uniform dispersion of Cu via the EDTA grafting method, which were evaluated for toluene catalytic combustion and exhibited outstanding catalytic activity and stability. The morphology, structure, surface properties of the catalysts was explored by X-ray diffraction (XRD), N_2 adsorption and desorption, high-resolution transmission electron microscope (HRTEM), Raman spectroscopy, hydrogen temperature programmed reduction (H_2-TPR) and so on. Moreover, through time-dependent in situ DRIFT spectra of the characteristic aromatic ring stretching vibrations, reaction mechanisms were explored on toluene catalytic combustion over the surface of Cu-CeO_x-MOF-0.2.

2. Results and Discussion

2.1. Preparation and Characterizations of Cu-CeO_x-MOF-n

2.1.1. Preparation of Cu-CeO_x-MOF-n

EDTA is a kind of grafting ligand with strong complexing ability. Despite of the successful EDTA grafting in Zr-MOF-808, the Ce-MOF-808 structure would be damaged due to the stronger EDTA elution effect of Ce [32,33]. We found through research that the EDTA grafting method could be extended to Ce-MOF-808 when the reaction time of the synthesis step was controlled under 15 min. As the result, the Ce-MOF-808 structure could be retained, and Cu could be successfully introduced with uniform dispersion.

The schematic illustration was shown in Figure 1. EDTA could be grafted on the framework by replacing formic acid and the maximum EDTA grafting amount could achieve twice as the molar quantity of Ce_6 clusters [28,29]. After grafting EDTA ligands on Ce-MOF-808, the Ce-MOF-808-EDTA precursor was able to stabilize copper species with different contents. In Cu-Ce-MOF-n, Cu was atomically dispersed in Ce-MOF-808 on account of the introduction by the chelation of EDTA. Herein, Cu-Ce-MOF-n was calcined at 500 °C in air atmosphere to obtain Cu-CeO_x-MOF-n catalysts with highly uniform Cu dispersion.

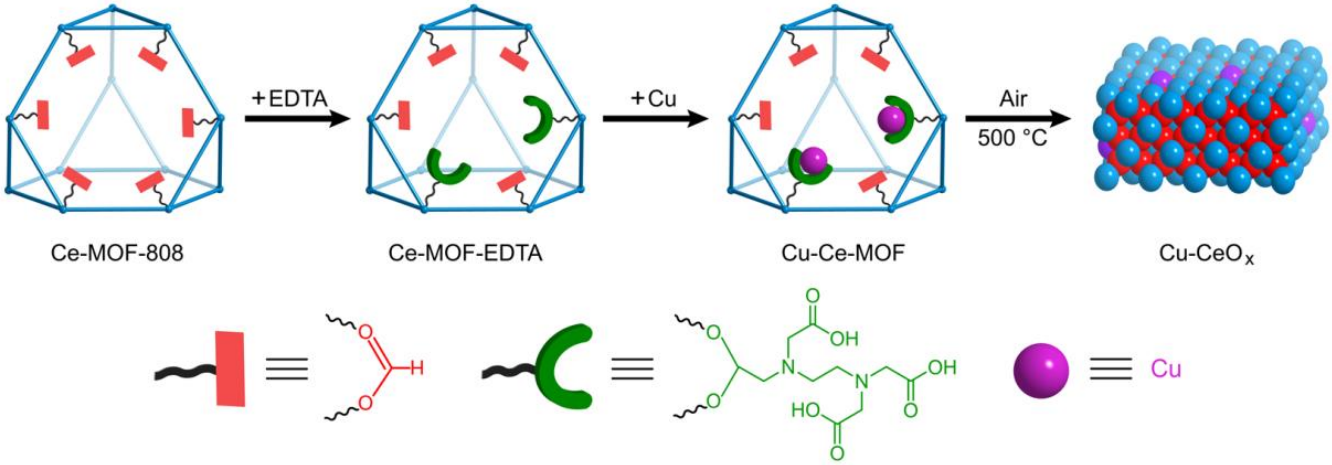

Figure 1. The schematic illustration of the Cu-CeO_x-MOF-n synthesis process.

2.1.2. X-Ray Diffraction (XRD)

XRD was implemented to confirm the anticipate crystal structure of Cu-Ce-MOF-n and Cu-CeO_x-MOF-n. MOF-808 was first proposed with Zr_6 cluster as the central metal cluster [34]. Due to the similarity between Ce and Zr, the structure of Ce-MOF-808 was similar to MOF-808 [35]. For Cu-Ce-MOF-n, characteristic diffraction peaks at 4.1°, 8.0° and 8.3° could be observed in Figure 2a, which were assigned to the (111), (311) and (222) facets of MOF-808, respectively [34]. This indicated that structures of Cu-Ce-MOF-n were not influenced by EDTA and Cu incorporation.

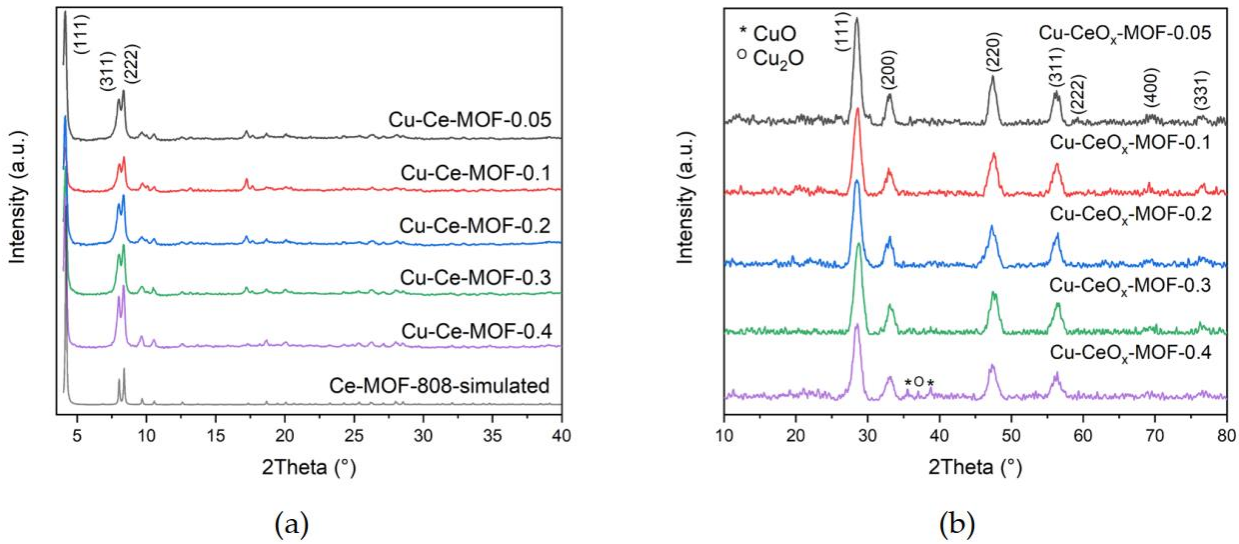

Figure 2. XRD patterns of (**a**) Cu-Ce-MOF-n and (**b**) Cu-CeO_x-MOF-n.

For Cu-CeO_x-MOF-n, the characteristic diffraction peaks attributed to the cubic CeO_2 phase (JCPDS Card No. 34-0394) were observed in all samples as shown in Figure 2b, displaying peaks at 28.6°, 33.1°, 47.3°, 56.4°, 59.3°, 69.6°, 76.7° and 79.1° (2θ) respectively, corresponding to the facets of (111), (200), (220), (311), (222), (400), (331) and (420). The result of particle sizes calculated by the most intensive characteristic peak (111) of CeO_2 was listed in Table 1, and the particle size distribution of particles was 6–8 nm. By contrast, the characteristic diffraction peaks associated with CuO were weak. The two relatively strong peaks at 35.5° and 38.7°, which corresponded to the (−111) and (111) facets of CuO (JCPDS Card No. 80-1916), were observed on Cu-CeO_x-MOF-0.4 and marked in Figure 2b,

suggesting the aggregation of CuO. In addition, it was noted that in the sample Cu-CeO_x-MOF-0.4, the peak of Cu_2O (111) facet appeared at 36.5° (JCPDS Card No. 65-3288), which indicated that Cu^+ and Cu^{2+} coexisted in this sample. Based on the above analyses, when Cu content was low ($n < 0.3$), Cu was uniformly dispersed on CeO_2 in Cu-CeO_x-MOF-n catalysts prepared by EDTA grafting method.

Table 1. ICP-AES, XRD, the N_2 adsorption and desorption, Raman, X-ray photoelectron spectroscopy (XPS) and H_2-TPR results of Cu-CeO_x-MOF-n.

n	ICP-AES	XRD	N_2 Adsorption and Desorption	Raman	XPS		H_2-TPR	
	m_{Cu}/m_{Ce}	D (nm)	SSA (m^2/g)	A_D/A_{F2g} (%)	$O_\alpha/(O_\alpha+O_\beta)$ (%)	$Ce^{3+}/(Ce^{3+}+Ce^{4+})$ (%)	$T_{Peak\ 1}$ (°C)	$T_{Peak\ 2}$ (°C)
0.05	0.053	8.0	54	8	18.7	21.3	/	178
0.1	0.105	6.9	67	9	19.3	21.4	144	177
0.2	0.122	6.6	57	13	20.7	22.4	145	174
0.3	0.147	6.9	61	9	18.5	21.5	163	191
0.4	0.225	6.6	57	8	17.5	21.0	178	211

2.1.3. N_2 Adsorption and Desorption Measurements and Thermogravimetry (TG)

Specific surface areas of Cu-CeO_x-MOF-n samples were investigated by N_2 adsorption and desorption isotherms (Table 1, Figure S2). In this work, the specific surface area (SSA) of Cu-CeO_x-MOF-n formed by EDTA grafting method were in the range of 54–67 m^2/g, showing no evident trend with different Cu content.

Considering that Cu-Ce-MOF-n samples were applied as precursors and required further calcination to generate transition metal oxide catalysts, TG experiment was indispensable. The TG curve of Cu-Ce-MOF-0.2 kept the mass constant above 400 °C (Figure S1), meaning that the calcination temperature (500 °C) in the catalyst synthesis process was adequate to form stable Cu-CeO_x-MOF-n.

2.1.4. Inductively Coupled Plasma-Atomic Emission Spectrometry (ICP-AES), Field Emission Scanning Electron Microscope (FESEM) and High-Resolution Transmission Electron Microscope (HRTEM) Analyses

To determine the content of Cu and Ce on Cu-CeO_x-MOF-n, ICP-AES was implemented. As shown in Table 1, the results revealed that the Cu/Ce mass ratio was 0.053, 0.105, 0.122, 0.147 and 0.225 with the increase of n, symbolizing the successful introduction of Cu into CeO_2 through the EDTA grafting method in this work. It was reported that the chelation efficiency of grafted EDTA on MOFs with heavy metal could reach 99% [29]. Compared to theoretical values, the Cu/Ce ratio values were basically the same in Cu-CeO_x-MOF-0.05, Cu-CeO_x-MOF-0.1 while obviously lower in Cu-CeO_x-MOF-0.2, Cu-CeO_x-MOF-0.3 and Cu-CeO_x-MOF-0.4. EDTA solution was usually used as an eluent for MOFs because of its strong cation chelation ability [32,33]. With high EDTA and Cu content, EDTA might cause more damages to the structure of Ce-MOF-808 during the ligand exchange period, resulting in insufficient EDTA ligands grafting on Ce-MOF-808.

FESEM images were used to intuitively scrutinize the microstructure of Cu-CeO_x-MOF-n catalysts. As the FESEM picture of Cu-CeO_x-MOF-0.2 shown in Figure 3a, the oxides, generated by the EDTA grafting method, were in the form of particles and there was obvious adhesion between particles. HRTEM was performed for element investigation of Cu-CeO_x-MOF-n (Figure 3b,c and Figure S3). A typically image of the Cu-CeO_x-MOF-0.2 sample was shown in Figure 3b and the (111), (200) and (220) facets of CeO_2 were marked. The average nanoparticle sizes of series samples were about 7 nm, which were consistent with the data calculated by XRD in Table 1. Besides, the (111) facet of Cu_2O (d = 0.25 nm) was found in Cu-CeO_x-MOF-0.4 (Figure 3c), while it was not observed in other samples (Figure S4). The energy dispersive X-ray spectroscopy (EDS) profiles of Ce, Cu and O in Figure 3e–g revealed the uniform dispersion of Cu on CeO_2.

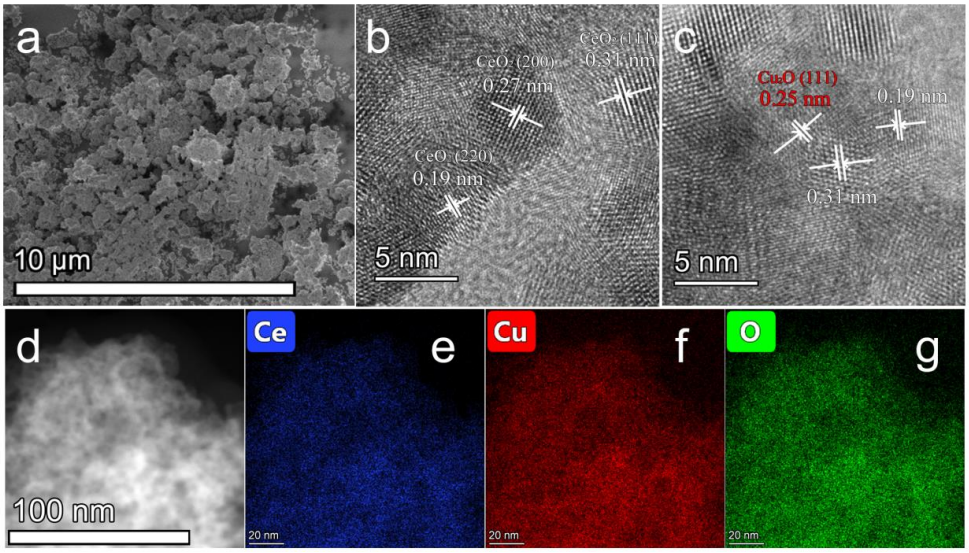

Figure 3. (**a**) FESEM image of Cu-CeO_x-MOF-0.2; (**b**,**c**) HRTEM image of Cu-CeO_x-MOF-0.2 and Cu-CeO_x-MOF-0.4 and (**d**–**g**) EDS mapping results of Cu-CeO_x-MOF-0.2 ((**e**) Ce, (**f**) Cu and (**g**) O).

2.1.5. Raman Spectroscopy and X-ray Photoelectron Spectroscopy (XPS)

For the purpose of more detailed insights on the surface defect, Cu-CeO_x-MOF-n catalysts were characterized by Raman spectroscopy (Figure 4). The most intensive bands at 464 cm^{-1} exhibited strong vibrations (F_{2g}) of CeO_2 cubic fluorite, while the bands at 600 cm^{-1} was ascribed to the defected-induced (D) mode of CeO_2 [36]. It was accepted that abundant oxygen vacancies in Ce-based catalysts would promote catalytic activity and the relative area ratio of A_D/A_{F2g} could be generally utilized to estimate oxygen vacancy concentration in the CeO_2 [37]. As calculated results demonstrated in Table 1, with the increase of Cu content in samples, A_D/A_{F2g} value ascended from 8% (Cu-CeO_x-MOF-0.05) to the maximum 13% (Cu-CeO_x-MOF-0.2) and then descended to 8% (Cu-CeO_x-MOF-0.4), implying a relatively significant increase in oxygen vacancy on Cu-CeO_x-MOF-0.2 compared to other samples. This indicated that the introduction of highly dispersed Cu could increase the amount of oxygen vacancies, and when the introduced Cu started to aggregate, the amount of oxygen vacancies would decrease [38].

The surface elemental compositions of Cu-CeO_x-MOF-n catalysts were investigated by XPS. Photoelectron peaks of Cu $2p_{3/2}$, binding energy from 930 to 940 eV, were further investigated. As Cu spectra shown in Figure 5a, in as-prepared Cu-CeO_x-MOF-n samples, the characteristic peaks were observed around 932.2 eV. As reported, binding energy related to Cu^{2+} characteristic peaks were assigned to locate at 934.5 eV and were higher than that corresponding to Cu^+ (932.5 eV) [39,40]. Furthermore, the weak intensities of the satellite peaks representing Cu^{2+} were found at 943 eV and 962 eV, indicated that the ratio of Cu^{2+} was low in all samples [41,42]. Copper with low valence was recognized as the reduction product by Ce^{3+} through the reaction: $Cu^{2+} + Ce^{3+} = Cu^+ + Ce^{4+}$. The above analyses proved the strong Cu–Ce interaction in Cu-CeO_x-MOF-n catalysts, which was resulted from the high dispersion of Cu in the precursor.

The Ce 3d spectra were also measured to obtain a better understanding of the catalyst surface environment, as shown in Figure 5b. According to previous reports, Ce 3d bands were generally divided into 8 [41] or 10 [27,43] peaks. In this work, these peaks were deconvoluted into 10 peaks and separated into two groups: (1) $3d_{5/2}$, whose corresponding peaks were labeled as V and (2) $3d_{3/2}$, whose relative peaks were labeled as U. From low binding energy to high ones, these peaks were denoted as V_0 (880.4 eV), V (881.7 eV), V′ (883.7 eV), V″ (888.3 eV) and V‴ (897.2 eV) and U_0 (898.7 eV), U (899.9 eV), U′ (901.9 eV), U″ (906.5 eV) and U‴ (915.6 eV), respectively. Among these characteristic peaks, V_0, V′, U_0 and U′ were ascribed to Ce^{3+}, and the others were assigned to Ce^{4+}. The proportion of Ce^{3+}

was associated with oxygen vacancies in the structure of CeO_2, which played a vital role in oxidation reaction. Therefore, catalysts with higher Ce^{3+} proportion were more beneficial for toluene catalytic combustion. The Ce^{3+}/Ce^{4+} ratios of Cu-CeO_x-MOF-n calculated by XPS were among the high value of 21.0–22.4%, with Cu-CeO_x-MOF-0.2 owning the highest ratio.

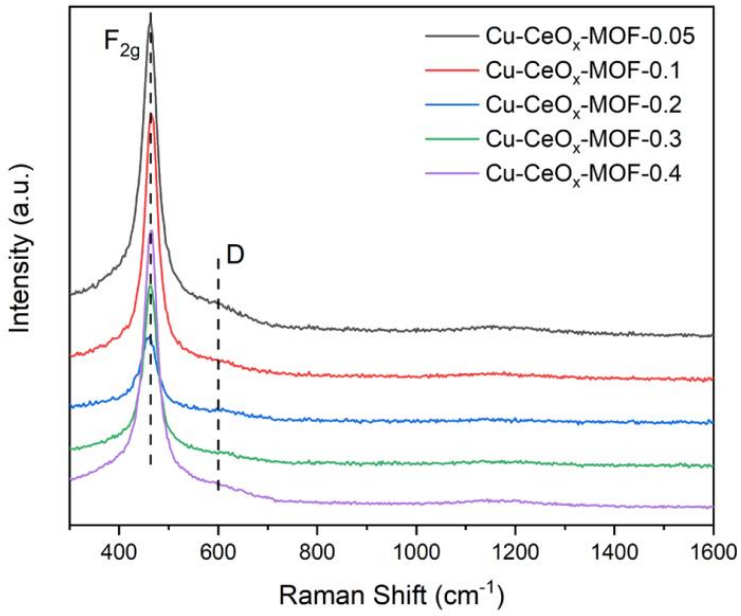

Figure 4. The Raman spectra curves of Cu-CeO_x-MOF-n samples.

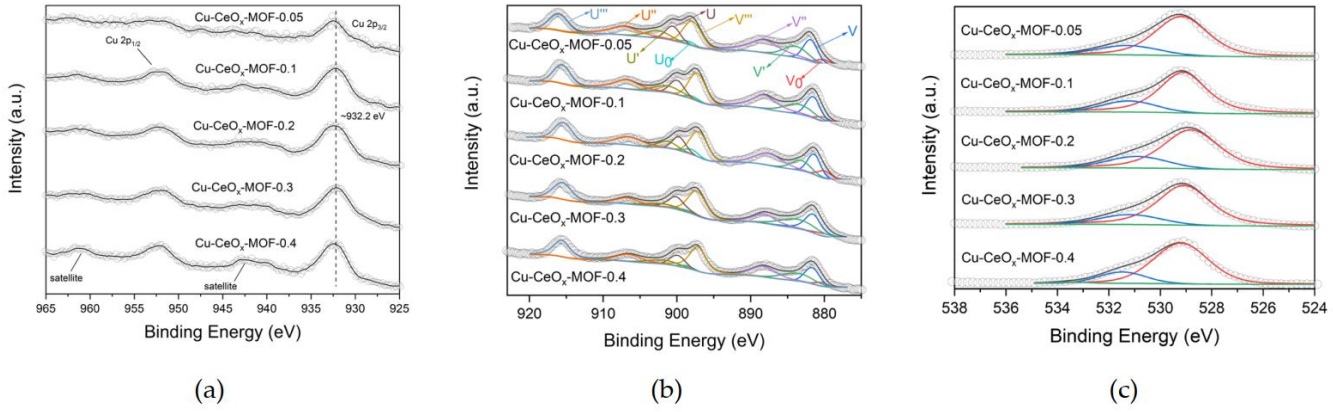

Figure 5. XPS spectra for (**a**) Cu 2p, (**b**) Ce 3d and (**c**) O 1s of Cu-CeO_x-MOF-n samples (circuits represent experimental data and lines represent smoothed or fitted data).

The O 1s bands were deconvoluted into two characteristic peaks in Figure 5c. The ones centered at 529.2 eV were assigned to lattice oxygen species (O_β), which were generally identified as O^{2-} in the catalyst lattice and had little participation in the reaction. The peaks at 531.7 eV were ascribed to surface oxygen species (O_α) including O_2^-, O_2^{2-}, O^-, etc., which could involve in redox reaction much further. The ratio of $O_\alpha/(O_\alpha+O_\beta)$ was regarded as an important parameter to evaluate the redox reactivity of catalysts. Higher ratio of $O_\alpha/(O_\alpha+O_\beta)$ suggested more active surface oxygen in catalysts and better catalytic activity. The $O_\alpha/(O_\alpha+O_\beta)$ ratios of Cu-CeO_x-MOF-n were listed in Table 1, ranging from 17.5% to 20.7%, with the highest value appeared on Cu-CeO_x-MOF-0.2, implying more favorable catalytic performances.

2.1.6. Hydrogen Temperature Programmed Reduction (H_2-TPR)

To better understand the reduction behavior over Cu-CeO_x-MOF-n, H_2-TPR was applied over these samples. Figure 6 exhibited the H_2-TPR profiles of the Cu-CeO_x-MOF-n catalysts, in which the position and intensity of the reductive peaks were determined after convolution.

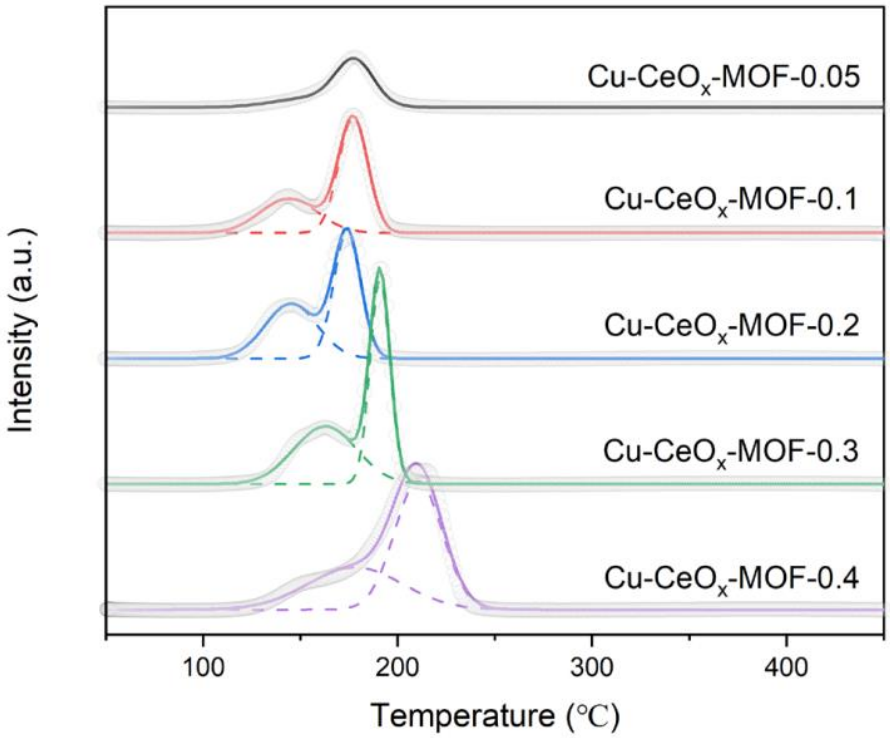

Figure 6. The H_2-TPR profiles of Cu-CeO_x-MOF-n samples (circuits represent experimental data and lines represent smoothed or fitted data).

It was generally accepted that reduction peaks of CuO were lower compared with 450 °C and reduction peaks attributed to CeO_2 were higher than 450 °C in the entire H_2-TPR profiles ranging from 50 to 900 °C (Figure S5). Due to the existence of Cu, which owned relatively stronger reducibility, only one typical broad and low peak of CeO_2 was clearly observed at 800 °C, which was ascribed to the reduction of bulk oxygen in CeO_2. There was no significant difference in reduction temperature of bulk oxygen in CeO_2 on series samples.

For the profound guidance of catalyst reactivity applying to toluene catalytic combustion, we placed emphasis on low-temperature reduction peaks, since lower reduction temperature meant catalysts were more easily reduced by H_2 and could more efficiently involved in the toluene combustion reaction further.

The H_2-TPR profile of Cu-CeO_x-MOF-n displayed two reduction peaks overlapped at the temperature range of 100–250 °C, which was assigned to the reduction of CuO in Cu-CeO_x-MOF-n. Compared to the temperature of pure CuO sample reduction peak (above 300 °C) [44,45], the lower temperature of reduction peaks in Cu-CeO_x-MOF-n samples indicated that strong interactions between Cu and Ce.

In addition, the peak below 250 °C could be principally divided into two Gaussian peaks, marked as Peak 1 and Peak 2, respectively and the positions were shown in Table 1. Peak 1 was assigned to well-dispersed superfine CuO_x nanoparticles, and Peak 2 was attributed to a strong Cu–Ce interaction, which was related to the catalytic activity [21]. It was deserved to mention that the reductive temperatures of Peak 1 on Cu-CeO_x-MOF-0.1 and Cu-CeO_x-MOF-0.2 were lower (144 °C and 145 °C respectively), indicating relatively stronger redox capacity at lower reaction temperature. Moreover, Cu-CeO_x-MOF-0.2 had

the lowest reductive temperature of Peak 2, which could also be assigned to its strong redox property. Evident shifts of Peak 2 positions were observed on Cu-CeO_x-MOF-0.3 and Cu-CeO_x-MOF-0.4. Since Cu^+ is more easily reduced than Cu^{2+}, the temperature shifts of Peak 2 in the samples indicated higher proportions of Cu^{2+}, which was consistent with the results of XPS [44,45]. In addition, considering that crystalline CuO was formed in Cu-CeO_x-MOF-0.4, the proportion of Peak 1 decreased and the broader Peak 2 width was regarded to be caused by the overlapping of crystalline CuO [40,46].

The above results show that Cu was highly dispersed on CeO_2 by EDTA grafting method at certain amount (n < 0.3). The strong interaction between Cu and Ce could increase the CeO_2 structural defect, which was beneficial to the formation of oxygen vacancies and O_α. These changes could enhance the catalytic activity of the oxide catalysts.

2.2. Catalytic Performance

The catalytic performances of VOCs combustion catalysts were normally evaluated by T_{50} and T_{90} (the reaction temperatures with toluene conversion of 50% and 90% respectively). As represented in Figure 7, the catalytic performance of the Cu-CeO_x-MOF-n catalysts was performed under toluene concentration 1000 ppm and weight hourly space velocity (WHSV) 60,000 mL/(g_{cat}·h), and the corresponding results were summarized in Table 2. Cu-CeO_x-MOF-0.2 exhibited the highest catalytic performance with T_{50} = 207 °C and T_{90} = 226 °C among all samples with different Cu content. The overall catalytic performance results showed that the samples with the most surface reactive oxygen species had the best catalytic activity. With the incorporation of Cu, the T_{90} of Cu-CeO_x-MOF-n declined obviously and the catalytic activity under high conversion enhanced significantly in comparison to CeO_2-MOF-808, whose T_{90} was tested 278 °C in our previous stage of work [22]. In addition, the Cu-CeO_x-MOF-0.2 catalysts had decent catalytic expression under different WHSVs (Figure 7b). Cu-CeO_x-MOF-0.2 displayed relatively satisfactory catalytic performances on toluene combustion compared previously reported various transition metal oxide catalysts that were summarized in Table 2.

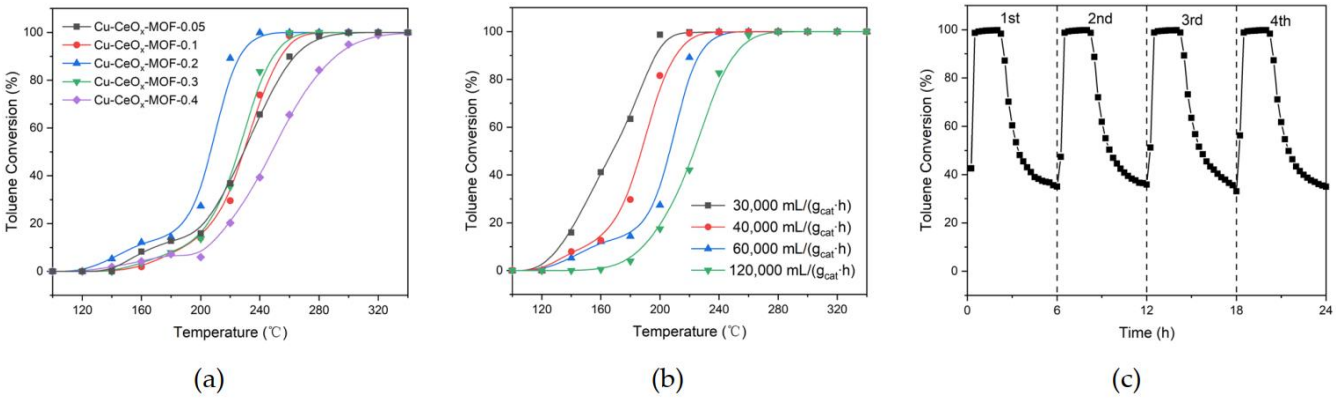

Figure 7. Toluene conversions at a reaction temperature over (**a**) Cu-CeO_x-MOF-n catalysts (60,000 mL/(g_{cat}·h)) and over (**b**) Cu-CeO_x-MOF-0.2 (from 30,000 mL/(g_{cat}·h) to 120,000 mL/(g_{cat}·h)) and (**c**) stability tests of Cu-CeO_x-MOF-0.2 in 200 °C and 240 °C.

Moreover, the catalytic stability test was conducted at several reaction temperature cycles under the same WHSV (60,000 mL/(g_{cat}·h)), and the results were illustrated in Figure 7c. Cu-CeO_x-MOF-0.2 catalyst exhibited remarkable stability in the whole test period and the catalytic activity could maintain the original high level after six consecutive rounds of circulation between 200 and 240 °C.

Taking the above results into consideration, Cu-CeO_x-MOF-n catalysts demonstrated outstanding catalytic activity and stability in the catalytic oxidation of toluene. The versatile advantages of Cu-CeO_x-MOF-n catalysts make them attractive for realistic environmental applications, particularly VOCs catalytic combustion.

Table 2. Toluene combustion catalytic activity summary of Cu-CeO_x.

Composition	Preparation Method	Toluene Concentration (ppm)	WHSV ($mL/g_{cat} \cdot h$)	T_{50} (°C)	T_{90} (°C)
Cu-CeO_x-0.05	MOF precursor via EDTA grafting method	1000	60,000	224	263
Cu-CeO_x-0.1		1000	60,000	224	254
Cu-CeO_x-0.2		1000	60,000	207	226
		1000	30,000	163	197
		1000	40,000	182	211
		1000	120,000	221	250
Cu-CeO_x-0.3		1000	60,000	222	249
Cu-CeO_x-0.4		1000	60,000	244	291
$Cu_{0.15}Ce_{0.85}$ [20]	combustion method	600	50,000	209	210
CuO-CeO_2 [47]	calcination	500	50,000	211	231
$Ce_{0.8}Cu_{0.2}O$ [45]	surfactant precipitation method	5000	9000	>250	>250
CeCu-HT [48]	hard-template method	10,000	66,000	221	223
$Ce_{0.4}Cu_{0.6}$ [9]	double redox method	500	50,000 h^{-1}	228	245
$CuCeZr_4$ [49]	sol-gel method	1500	24,000 h^{-1}	183	219

2.3. In Situ DRIFTS Study of Toluene Catalytic Combustion

In order to monitor the involved intermediates and verify the reaction mechanism of toluene combustion on the catalyst surface, in situ DRIFTS tests were performed on Cu-CeO_x-MOF-0.2. After pretreatment, toluene/He passed through the samples and the spectra were recorded until 30.5 min. Then O_2/He inlet was introduced and the changes were also recorded.

Figure 8a showed in situ DRIFT spectra on Cu-CeO_x-MOF-0.2 over time after toluene introduction. The position, assignment and possible attribution of the infrared peaks in the experiments were listed in Table 3. It could be clearly concluded that critical intermediates including benzyl (3066 cm^{-1}), benzyl alcohol (1158 cm^{-1}, 1098 cm^{-1} and 1069 cm^{-1}), benzaldehyde (1647 cm^{-1}), benzoic acid (1521 cm^{-1}), phenol (1242 cm^{-1}), maleic anhydride (1960 cm^{-1}, 1917 cm^{-1}, 1813 cm^{-1}, 1740 cm^{-1} and 1307 cm^{-1}) and formic acid (1410 cm^{-1} and 1558 cm^{-1}) were formed during toluene catalytic combustion. The catalytic reaction process could be reasonably deduced: (1) toluene was first adsorbed on the catalyst surface; (2) toluene dehydrogenated to benzyl; (3) benzyl was oxidized to benzyl alcohol, benzaldehyde and benzoate in sequence; (4) decarboxylation procedure; (5) aromatic ring was oxidized to maleic anhydride; (6) formate was formed on catalyst surface and (7) formate finally separated in the form of CO_2. By comparing the intensity of each peak of infrared diffuse reflectance test results, it could be seen that although the vibration peak of intermediate product maleic anhydride could be detected on Cu-CeO_x-MOF-0.2, its intensity was relatively low, which indicated that maleic anhydride transformed rapidly on the surface of the catalyst. On the other hand, the peak intensities of benzene ring and carboxylic acid were higher in the whole spectrum, which implied that the ring opening of benzene ring and the oxidation of carboxylic acid were important intermediate steps of the reaction, which was consistent with the previous report [50].

Figure 8b showed more detailed spectra (from 1650 to 1350 cm^{-1}) over Cu-CeO_x-MOF-0.2 to concentrate on the vibration of aromatic ring and carboxylate. Aromatic rings substances (at 1440 cm^{-1}, 1498 cm^{-1}, 1574 cm^{-1} and 1593 cm^{-1}) were distinctly observed on Cu-CeO_x-MOF-0.2. Apart from these, two groups of vibration peaks were assigned to benzoate (at 1397 cm^{-1} and 1527 cm^{-1}) and farmate (at 1412 cm^{-1} and 1555 cm^{-1}) respectively. Δv values of asymmetric and symmetric v(C=O) stretching vibration were 130 cm^{-1} and 143 cm^{-1} respectively, close to the free ion values. This indicated that the carboxylate ions bonded with metal ions on the surface of Cu-CeO_x-MOF-0.2 with a bridging structure. Aromatic ring opening was considered as one of the rate-determine steps during toluene catalytic combustion. Benzoate was produced before ring opening while formate was deep oxidized after ring opening. As time went on, the peak intensity

attributed to formate increased, indicating that formate gradually accumulated on the surface of catalyst after aromatic ring opening. Thus, not only benzoate, but also formate was an important intermediate during catalytic combustion of toluene.

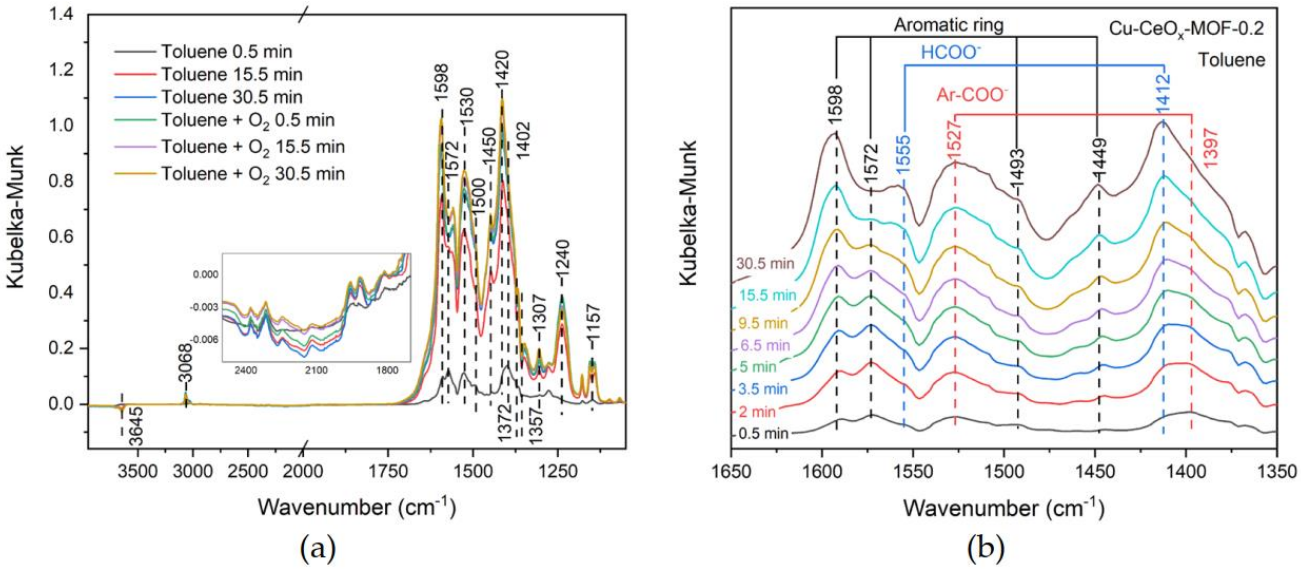

Figure 8. (**a**) In situ DRIFTS and (**b**) detailed DRIFTS between 1650 and 1350 cm^{-1} over Cu-CeO_x-MOF-0.2 after toluene introduction.

Table 3. The position, assignment and corresponding species of the infrared peaks in the experiment.

Wavenumber/cm^{-1}	Assignment	Corresponding Species
1158, 1098, 1069	C–O stretching vibration	benzyl alcohol [50]
1180	antisymmetric Ar–C stretching vibration	aromatic ring (fingerprint region) [51]
1242	C–O stretching vibration (phenolics)	phenol [52]
1397, 1527; 1412, 1555	symmetric C–O stretching vibration and antisymmetric C–O stretching vibration (carboxylate)	carboxylate [53,54]
1593, 1574, 1498, 1440	C=C skeleton vibration	aromatic ring [55,56]
1647	C=O stretching vibration (aromatic aldehydes)	benzaldehyde [57]
1960, 1917, 1813, 1740, 1307	symmetric and antisymmetric C=O stretching vibration (cyclic anhydrides)	maleic anhydride [30,58]
2320	antisymmetric CO_2 stretching vibration	CO_2 [59]
3066	C_{sp2}–H stretching vibration	aromatic ring or benzyl [60,61]

After introduction of O_2/He, the spectra of Cu-CeO_x-MOF-0.2 over time were recorded and shown in Figure S6. The main peak position of the catalyst showed unchanged, which suggested that the introduction of gaseous O_2 had no effect on the reaction path of the catalyst. The intensity variation of each species was also quite small, and the intensity of infrared vibration peak of benzene ring and carboxylic acid did not decrease, which indicated that the introduction of gaseous O_2 did not lead to faster desorption or reaction of the intermediates. The catalytic combustion of toluene mainly consumed lattice oxygen over Cu-CeO_x-MOF-0.2, which was consistent with MvK mechanism.

Based on the above analysis, it was speculated that toluene catalytic combustion started from the oxidation of methyl group of toluene over Cu-CeO_x-MOF-0.2. The illustration diagram was shown in Figure 9. Toluene was gradually oxidized to benzyl alcohol, benzaldehyde, benzoate, phenol, maleic anhydride, formate and finally to carbon dioxide and water. In the whole oxidation process, the opening of benzene ring or the deep oxidation of carboxylate was the important rate determining steps. The catalytic

combustion of toluene over Cu-CeO_x-MOF-0.2 conformed to MvK mechanism, and the oxidation of toluene was mainly carried out by lattice oxygen.

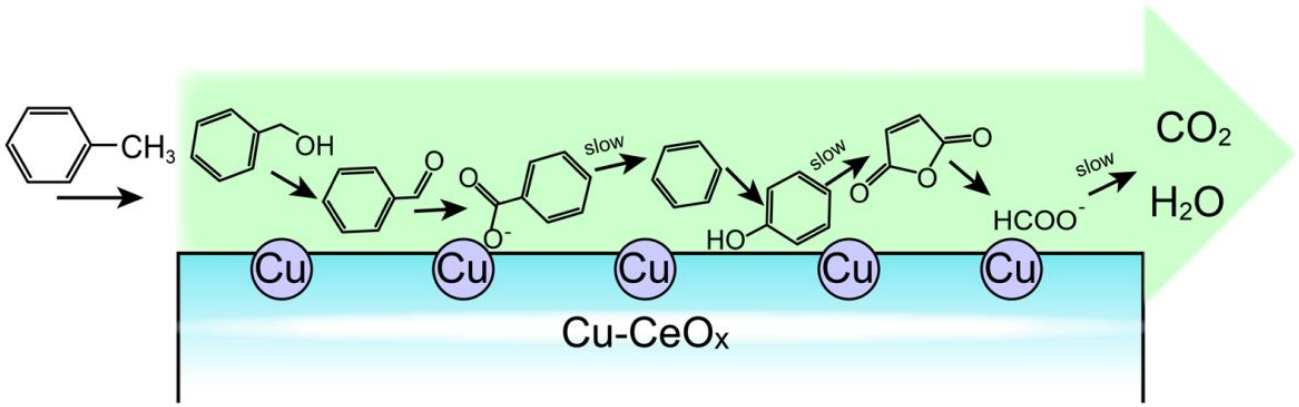

Figure 9. Illustration diagram of toluene catalytic combustion over Cu-CeO_x-MOF-0.2.

3. Experimental Section

3.1. Materials

N,*N*-dimethylformamide (DMF), 1,3,5-benzenetricarboxylic acid (H_3BTC), ethylenediaminetetraacetic acid disodium salt (EDTA-2Na) and $CuAc_2 \cdot H_2O$ were purchased from Sinopharm Chemical Reagent Co., Ltd. (Shanghai, China) $(NH_4)_2Ce(NO_3)_6$ was purchased from Macklin Biochemical Co., Ltd. (Shanghai, China). Deionized water was obtained through an ultra-pure water purification system. All the reagents were analytically pure (AR grade) and used without further purification in this work.

3.2. Catalyst Preparation

3.2.1. Synthesis of Ce-MOF-808

Ce-MOF-808 was synthesized with the reference to previous articles [35] and scaled up in this work. In brief, 12 mL H_3-BTC solution (0.088 mol/L) was dissolved in DMF. Then 6 mL $(NH_4)_2Ce(NO_3)_6$ water solution (0.533 mol/L) and 2.57 mL formic acid (98%) were added into a 50 mL sealed glass bottle. After heated at 100 °C for 10 min, the suspension was cooled and centrifuged. The yellow precipitate (Ce-MOF-808) was washed with DMF and acetone three times each and afterwards dried in a vacuum at 90 °C overnight.

3.2.2. Synthesis of Cu-Ce-MOF-n

Ce-MOF-808 (2 g) was dispersed into deionized water in a 50 mL sealed glass bottle. After 10 min stirring, 20 mL EDTA solution with certain concentration was added into the bottle and stirred for another 5 min. After centrifugation at 10,000 rpm for 10 min, the precipitate was washed with 15 mL deionized water three times and light brown powder (Ce-MOF-EDTA) was obtained. $CuAc_2 \cdot H_2O$ with equal molar ratio of EDTA was dissolved into 20 mL deionized water. Put light brown powder into the solution with continuously stirring for 4 h at the room temperature. After centrifugation, the deposits were washed with 15 mL deionized water and acetone three times each, and then dried at 90 °C. The products were denoted as Cu-Ce-MOF-n, where n represented the amount of copper acetate feeding, $n = m_{Cu}/m_{Ce}$ (m_{Cu}: mass of Cu, m_{Ce}: mass of Ce). The inventory ratings of EDTA-2Na and $CuAc_2 \cdot H_2O$ were listed in Table S1.

3.2.3. Synthesis of Cu-CeO_x-MOF-n

Cu-Ce-MOF-n was calcined at 500 °C in air for 4 h in the muffle furnace with heating rate 2 °C/min, and then cooled to room temperature. The prepared catalysts were denoted as Cu-CeO_x-MOF-n.

3.3. Catalyst Characterization

The powder X-ray diffractometer (D8 ADVANCE and DAVINCI DESIGN diffractometer, Bruker, Madison, WI, USA) equipped with Cu Kα radiation (λ = 0.154 nm, 40 kV, 40 mA) was operated. XRD patterns were recorded at a rotation speed of 12°/min with the step of 0.05°. The N_2 adsorption and desorption experiments of Cu-Ce-MOF-n samples were tested at 77 K on an automated analyzer (Quadrasorb evo, Anton Paar, Graz, Austria). Cu-CeO_x-MOF-n samples were conducted by another equipment (Tristar II 3020 adsorption instrument, Micromeritics, Norcross, GA, USA) under the same condition. Inductively coupled plasma-atomic emission spectrometry (ICP-AES) was employed on an atomic emission spectrometer (Optima 8000, Perkin Elmer, Waltham, MA, USA). The oxide samples were dissolved with the mixture of concentrated HCl and 30% H_2O_2 and then diluted before testing. Field emission scanning electron microscope (FESEM) experiments of oxide samples were implemented (Nova NanoSem 450, FEI, Hillsboro, OR, USA), and corresponding energy dispersive X-ray spectroscopy (EDS) analysis including elements of Cu, Ce and O was carried out on a silicon drift detector (X-max^N 80T, Oxford Instruments, Oxfordshire, UK). High resolution transmission electron microscope (HRTEM) experiments of Cu-CeO_x-MOF-n samples were performed (Talos F200X G2, FEI, Waltham, MA, USA) and corresponding energy dispersive X-ray spectroscopy (EDS) analysis was implemented (Quantax 400 detector, Bruker, Madison, WI, USA). X-ray photoelectron spectroscopy (XPS) spectra were obtained (PHI 5000, ULVCA-PHI, Chanhassen, MN, USA) with Cu Kα radiation to investigate surface compositions and elemental valence states of samples. Raman spectra were gathered from a laser microscopic confocal Raman spectrometer with λ = 532 nm (XploRA, Horiba, Nagoya, Japan). Hydrogen temperature programmed reduction (H_2-TPR) was tested on a chemisorption analyzer (Auto Chem II 2920, Micromeritics, Norcross, GA, USA). For H_2-TPR testing, the sample (100 mg) was pretreated in pure He (30 mL/min) at 300 °C for 30 min and then cooled to room temperature. The sample was then reduced in 5% H_2/He with temperature ramped up at 10 °C/min to 900 °C. In situ DRIFTS measurements were implemented on a spectrometer (Nicolet 6700, Thermo Fisher Scientific, Waltham, MA, USA). All in situ DRIFT spectra were accumulated 64 scans per minute at 4 cm^{-1} resolution with the range from 4000 to 1000 cm^{-1}. The data were processed by OMNIC. Prior to each test, each sample was pretreated at 300 °C under He (30 mL/min) for 1 h, then treated at 250 °C under 5% O_2/He (20 mL/min) for 1 h and finally switched to He to obtain a background spectrum, which should be deducted from the sample spectra. For testing, the mixture of toluene and He was introduced into the chamber through bubbling method, passing He (3 mL/min) into toluene placing in the ice-water bath. After 30 s influx, sample data was collected every 1.5 min during first 15 min and then the sampling interval was prolonged to 3 min until 30.5 min. Afterwards, 5% O_2/He (27 mL/min) was introduced and after 0.5 min, sample data was obtained every 1.5 min during first 15 min and then every 3 min until total 61 min.

3.4. Catalytic Activity Measurements

Catalytic performance for toluene catalytic oxidation reactions was carried out in a fixed-bed reactor. The catalyst (100 mg, 40–60 mesh) mixed with quartz sand were loaded in quartz reaction tube (length = 405 mm, i.d. = 8 mm). A high-pure air stream passed through toluene at 2 °C for feeding and another high-pure air flow was added for dilution, adjusting the reactant feed at 1000 ppm toluene. Before testing, the catalyst was pretreated in the reactant flow at 300 °C for 1 h. The temperature for the test ranged from 100 to 400 °C and the samples were taken every 20 °C with 1 h equilibrium interval. The total flow rate was 100 mL/min and corresponding weight hourly space velocity (WHSV) was 60,000 mL/(g_{cat}·h), calculated by the formula:

$$WHSV = \frac{\text{the gas total flow rate (mL/h)}}{\text{the mass of the catalyst (g)}}$$

In the tests of WHSV impacts, the WHSV was varied from 30,000 to 120,000 mL/(g_{cat}·h), maintaining the toluene content at 1000 ppm. The stability test was carried out at WHSV = 60,000 mL/(g_{cat}·h). The test temperature was maintained at 240 °C for 2 h, then cooled to 180 °C for 2 h, and the cycle test was conducted for 6 times. The reaction products were analyzed online performing on Trace GC Ultra gas chromatograph, Thermo Fisher Scientific, Milan, Italy, equipped with a Plot Q column a flame ionization detector (FID) detector. No production of organic byproducts was detected during the test.

The toluene conversion percentage was obtained utilizing the following formula:

$$\text{Toluene Conversion} = \frac{C_{in} - C_{out}}{C_{in}} \times 100\%$$

where C_{in} and C_{out} corresponded to the concentration of toluene inlet and outlet in a steady state, respectively.

4. Conclusions

In summary, through the improved EDTA grafting method, high-performance Cu-CeO_x-MOF-n catalysts with different Cu content were synthesized on the basis of Ce-MOF-808. Beneficial from the EDTA grafting method, the highly dispersed Cu showed strong interaction with CeO_2. Based on the investigation of Cu content, Cu-CeO_x-MOF-0.2 exhibited more favorable catalytic activity and stability in toluene combustion among series samples. The HRTEM and FESEM images revealed uniform Cu dispersion of Cu-CeO_x-MOF-0.2; XPS and Raman spectra indicated larger amounts of active surface oxygen. The T_{90} of Cu-CeO_x-MOF-0.2 was 226 °C at 60,000 mL/(g_{cat}·h) and the catalytic activity remained at a considerably high level during the temperature fluctuation tests. On the basis of the in situ DRIFTS studies, aromatic ring opening or deep oxidation of carboxylate was considered as the rate-limiting step. The lattice oxygen of the catalyst oxidized toluene directly, and the reaction conformed to the MvK mechanism.

Therefore, the discovery of promising Cu-CeO_x-MOF-n catalysts in this work may develop EDTA grafting method for the synthesis of highly active catalysts with greatly uniform dispersion for the second component for VOCs catalytic oxidation in realistic environmental applications, and unveil a new perspective for the process investigation via in situ DRIFTS.

Supplementary Materials: The following are available online at https://www.mdpi.com/article/10.3390/catal11040519/s1, Table S1: the thermogravimetry curves of Cu-Ce-MOF-n, Figure S1: the thermogravimetry curves of Cu-Ce-MOF-0.2, Figure S2: the N_2 adsorption and desorption isotherms of Cu-CeO_x-MOF-n, Figure S3: the HRTEM images of (a) Cu-CeO_x-MOF-0.05, (b) Cu-CeO_x-MOF-0.1 and (c) Cu-CeO_x-MOF-0.3, Figure S4: the FESEM images of (a) Cu-CeO_x-MOF-0.05, (b) Cu-CeO_x-MOF-0.1, (c) Cu-CeO_x-MOF-0.3, (d) Cu-CeO_x-MOF-0.4 and (e-h) EDS mapping results of Cu-CeO_x-MOF-0.2 ((f) Cu, (g) Ce, and (h) O), Figure S5: the whole H_2-TPR profiles of Cu-CeO_x-MOF-n and Figure S6: In situ DRIFTS results after O_2 introduction over Cu-CeO_x-MOF-0.2 at the range of 1650 cm^{-1}–1350 cm^{-1}.

Author Contributions: Data curation, W.S. (Wenjie Sun) and Y.H.; Funding acquisition, H.X. and W.S. (Wei Shen); Investigation, W.S. (Wenjie Sun); Writing—original draft, W.S. (Wenjie Sun), Y.H. and X.L.; Writing—review and editing, Z.H., H.X. and W.S. (Wei Shen). All authors have read and agreed to the published version of the manuscript.

Funding: This research was funded by Shanghai Science and Technology Committee (Grant 14DZ2273900).

Conflicts of Interest: The authors declare no conflict of interest.

References

1. Hui, L.; Liu, X.; Tan, Q.; Feng, M.; An, J.; Qu, Y.; Zhang, Y.; Jiang, M. Characteristics, source apportionment and contribution of VOCs to ozone formation in Wuhan, Central China. *Atmos. Environ.* **2018**, *192*, 55–71. [CrossRef]
2. Yang, Y.; Liu, X.; Qu, Y.; Wang, J.; An, J.; Zhang, Y.; Zhang, F. Formation mechanism of continuous extreme haze episodes in the megacity Beijing, China, in January 2013. *Atmos. Res.* **2015**, *155*, 192–203. [CrossRef]

3. Kinney, P.L. Interactions of Climate Change, Air Pollution, and Human Health. *Curr. Environ. Health Rep.* **2018**, *5*, 179–186. [CrossRef] [PubMed]
4. Sarigiannis, D.A.; Karakitsios, S.P.; Gotti, A.; Liakos, I.L.; Katsoyiannis, A. Exposure to major volatile organic compounds and carbonyls in European indoor environments and associated health risk. *Environ. Int.* **2011**, *37*, 743–765. [CrossRef]
5. Wang, Y.; Li, Z.; Tang, C.; Ren, H.; Zhang, Q.; Xue, M.; Xiong, J.; Wang, D.; Yu, Q.; He, Z.; et al. Few-layered mesoporous graphene for high-performance toluene adsorption and regeneration. *Environ. Sci. Nano* **2019**, *6*, 3113–3122. [CrossRef]
6. Malakar, S.; Saha, P.D.; Baskaran, D.; Rajamanickam, R. Comparative study of biofiltration process for treatment of VOCs emission from petroleum refinery wastewater—A review. *Environ. Technol. Innov.* **2017**, *8*, 441–461. [CrossRef]
7. Palma, V.; Cortese, M.; Renda, S.; Ruocco, C.; Martino, M.; Meloni, E. A Review about the Recent Advances in Selected NonThermal Plasma Assisted Solid-Gas Phase Chemical Processes. *Nanomaterials* **2020**, *10*, 1596. [CrossRef]
8. Zhong, J.; Zeng, Y.; Chen, D.; Mo, S.; Zhang, M.; Fu, M.; Wu, J.; Su, Z.; Chen, P.; Ye, D. Toluene oxidation over Co^{3+}-rich spinel Co_3O_4: Evaluation of chemical and by-product species identified by in situ DRIFTS combined with PTR-TOF-MS. *J. Hazard. Mater.* **2020**, *386*, 121957. [CrossRef]
9. Zeng, Y.; Haw, K.-G.; Wang, Z.; Wang, Y.; Zhang, S.; Hongmanorom, P.; Zhong, Q.; Kawi, S. Double redox process to synthesize CuO–CeO_2 catalysts with strong Cu–Ce interaction for efficient toluene oxidation. *J. Hazard. Mater.* **2021**, *404*, 124088. [CrossRef]
10. Piumetti, M.; Fino, D.; Russo, N. Mesoporous manganese oxides prepared by solution combustion synthesis as catalysts for the total oxidation of VOCs. *Appl. Catal. B Environ.* **2015**, *163*, 277–287. [CrossRef]
11. Xu, W.; Xiao, K.; Lai, S.; Liang, J.; Jiang, X.; Liu, Z.; Li, F.; Zhang, Y.; Wu, X.; Zhou, X. Designing a dumbbell-brush-type Co_3O_4 for efficient catalytic toluene oxidation. *Catal. Commun.* **2020**, *140*, 106005. [CrossRef]
12. Li, Y.; Han, W.; Wang, R.; Weng, L.-T.; Serrano-Lotina, A.; Banares, M.A.; Wang, Q.; Yeung, K.L. Performance of an aliovalent-substituted CoCeOx catalyst from bimetallic MOF for VOC oxidation in air. *Appl. Catal. B Environ.* **2020**, *275*, 119121. [CrossRef]
13. Kamal, M.S.; Razzak, S.A.; Hossain, M.M. Catalytic oxidation of volatile organic compounds (VOCs)—A review. *Atmos. Environ.* **2016**, *140*, 117–134. [CrossRef]
14. Wang, P.; Wang, J.; An, X.; Shi, J.; Shangguan, W.; Hao, X.; Xu, G.; Tang, B.; Abudula, A.; Guan, G. Generation of abundant defects in Mn-Co mixed oxides by a facile agar-gel method for highly efficient catalysis of total toluene oxidation. *Appl. Catal. B Environ.* **2021**, *282*, 119560. [CrossRef]
15. Huang, H.; Xu, Y.; Feng, Q.; Leung, D.Y.C. Low temperature catalytic oxidation of volatile organic compounds: A review. *Catal. Sci. Technol.* **2015**, *5*, 2649–2669. [CrossRef]
16. Montini, T.; Melchionna, M.; Monai, M.; Fornasiero, P. Fundamentals and Catalytic Applications of CeO_2-Based Materials. *Chem. Rev.* **2016**, *116*, 5987–6041. [CrossRef] [PubMed]
17. Miao, C.; Liu, J.; Zhao, J.; Quan, Y.; Li, T.; Pei, Y.; Li, X.; Ren, J. Catalytic combustion of toluene over CeO_2-CoO(x)composite aerogels. *New J. Chem.* **2020**, *44*, 11557–11565. [CrossRef]
18. Zhou, J.; Wang, D.; Wu, G.; Fang, N.; Song, X.; Li, J.; Chen, J.; Liu, Y.; Guo, J.; Chu, Y. Enhanced Catalytic Combustion Performance of Toluene over a Novel Co–CeOx Monolith Catalyst. *Energy Fuels* **2021**, *35*, 6190–6201. [CrossRef]
19. Lu, J.; Wang, J.; Zou, Q.; He, D.; Zhang, L.; Xu, Z.; He, S.; Luo, Y. Unravelling the Nature of the Active Species as well as the Doping Effect over Cu/Ce-Based Catalyst for Carbon Monoxide Preferential Oxidation. *ACS Catal.* **2019**, *9*, 2177–2195. [CrossRef]
20. Delimaris, D.; Ioannides, T. VOC oxidation over CuO–CeO_2 catalysts prepared by a combustion method. *Appl. Catal. B Environ.* **2009**, *89*, 295–302. [CrossRef]
21. Zhou, G.; Lan, H.; Song, R.; Xie, H.; Du, Q. Effects of preparation method on CeCu oxide catalyst performance. *RSC Adv.* **2014**, *4*, 50840–50850. [CrossRef]
22. Sun, W.; Li, X.; Sun, C.; Huang, Z.; Xu, H.; Shen, W. Insights into the Pyrolysis Processes of Ce-MOFs for Preparing Highly Active Catalysts of Toluene Combustion. *Catalysts* **2019**, *9*, 682. [CrossRef]
23. Liu, H.; Zhang, S.; Liu, Y.; Yang, Z.; Feng, X.; Lu, X.; Huo, F. Well-Dispersed and Size-Controlled Supported Metal Oxide Nanoparticles Derived from MOF Composites and Further Application in Catalysis. *Small* **2015**, *11*, 3130–3134. [CrossRef] [PubMed]
24. Das, R.; Pachfule, P.; Banerjee, R.; Poddar, P. Metal and metal oxide nanoparticle synthesis from metal organic frameworks (MOFs): Finding the border of metal and metal oxides. *Nanoscale* **2012**, *4*, 591–599. [CrossRef] [PubMed]
25. Zhao, S.-N.; Song, X.-Z.; Song, S.-Y.; Zhang, H.-J. Highly efficient heterogeneous catalytic materials derived from metal-organic framework supports/precursors. *Coord. Chem. Rev.* **2017**, *337*, 80–96. [CrossRef]
26. Wang, H.; Liu, M.; Guo, S.; Wang, Y.; Han, X.; Bai, Y. Efficient oxidation of o-xylene over CeO_2 catalyst prepared from a Ce-MOF template: The promotion of K+ embedding substitution. *Mol. Catal.* **2017**, *436*, 120–127. [CrossRef]
27. Chen, X.; Chen, X.; Yu, E.; Cai, S.; Jia, H.; Chen, J.; Liang, P. In situ pyrolysis of Ce-MOF to prepare CeO_2 catalyst with obviously improved catalytic performance for toluene combustion. *Chem. Eng. J.* **2018**, *344*, 469–479. [CrossRef]
28. Peng, Y.; Huang, H.; Zhang, Y.; Kang, C.; Chen, S.; Song, L.; Liu, D.; Zhong, C. A versatile MOF-based trap for heavy metal ion capture and dispersion. *Nat. Commun.* **2018**, *9*, 187. [CrossRef]
29. Li, J.; Huang, H.; Liu, P.; Song, X.; Mei, D.; Tang, Y.; Wang, X.; Zhong, C. Metal-organic framework encapsulated single-atom Pt catalysts for efficient photocatalytic hydrogen evolution. *J. Catal.* **2019**, *375*, 351–360. [CrossRef]

30. Zhong, J.; Zeng, Y.; Zhang, M.; Feng, W.; Xiao, D.; Wu, J.; Chen, P.; Fu, M.; Ye, D. Toluene oxidation process and proper mechanism over Co_3O_4 nanotubes: Investigation through in-situ DRIFTS combined with PTR-TOF-MS and quasi in-situ XPS. *Chem. Eng. J.* **2020**, *397*, 125375. [CrossRef]
31. Wang, Q.; Yeung, K.L.; Banares, M.A. Operando Raman-online FTIR investigation of ceria, vanadia/ceria and gold/ceria catalysts for toluene elimination. *J. Catal.* **2018**, *364*, 80–88. [CrossRef]
32. Babazadeh, M.; Hosseinzadeh-Khanmiri, R.; Abolhasani, J.; Ghorbani-Kalhor, E.; Hassanpour, A. Solid phase extraction of heavy metal ions from agricultural samples with the aid of a novel functionalized magnetic metal-organic framework. *RSC Adv.* **2015**, *5*, 19884–19892. [CrossRef]
33. Ghorbani-Kalhor, E. A metal-organic framework nanocomposite made from functionalized magnetite nanoparticles and HKUST-1 (MOF-199) for preconcentration of Cd(II), Pb(II), and Ni(II). *Mikrochim. Acta* **2016**, *183*, 2639–2647. [CrossRef]
34. Furukawa, H.; Gándara, F.; Zhang, Y.-B.; Jiang, J.; Queen, W.L.; Hudson, M.R.; Yaghi, O.M. Water Adsorption in Porous Metal–Organic Frameworks and Related Materials. *J. Am. Chem. Soc.* **2014**, *136*, 4369–4381. [CrossRef] [PubMed]
35. Lammert, M.; Glissmann, C.; Reinsch, H.; Stock, N. Synthesis and Characterization of New Ce(IV)-MOFs Exhibiting Various Framework Topologies. *Cryst. Growth Des.* **2017**, *17*, 1125–1131. [CrossRef]
36. Schilling, C.; Hofmann, A.; Hess, C.; Ganduglia-Pirovano, M.V. Raman Spectra of Polycrystalline CeO_2: A Density Functional Theory Study. *J. Phys. Chem. C* **2017**, *121*, 20834–20849. [CrossRef]
37. Su, Z.; Yang, W.; Wang, C.; Xiong, S.; Cao, X.; Peng, Y.; Si, W.; Weng, Y.; Xue, M.; Li, J. Roles of Oxygen Vacancies in the Bulk and Surface of CeO_2 for Toluene Catalytic Combustion. *Environ. Sci. Technol.* **2020**, *54*, 12684–12692. [CrossRef]
38. Shan, W.J.; Shen, W.J.; Li, C. Structural characteristics and redox behaviors of $Ce_{1-x}Cu_xO_y$ solid solutions. *Chem. Mater.* **2003**, *15*, 4761–4767. [CrossRef]
39. Yin, M.; Wu, C.K.; Lou, Y.B.; Burda, C.; Koberstein, J.T.; Zhu, Y.M.; O'Brien, S. Copper oxide nanocrystals. *J. Am. Chem. Soc.* **2005**, *127*, 9506–9511. [CrossRef]
40. Luo, Y.; Wang, K.; Xu, Y.; Wang, X.; Qian, Q.; Chen, Q. The role of Cu species in electrospun CuO-CeO_2 nanofibers for total benzene oxidation. *New J. Chem.* **2015**, *39*, 1001–1005. [CrossRef]
41. Zeng, Y.; Wang, Y.; Song, F.; Zhang, S.; Zhong, Q. The effect of CuO loading on different method prepared CeO_2 catalyst for toluene oxidation. *Sci. Total Environ.* **2020**, *712*, 135635. [CrossRef]
42. Hocevar, S.; Krasovec, U.O.; Orel, B.; Arico, A.S.; Kim, H. CWO of phenol on two differently prepared CuO-CeO_2 catalysts. *Appl. Catal. B Environ.* **2000**, *28*, 113–125. [CrossRef]
43. Wang, Q.; Li, Z.; Banares, M.A.; Weng, L.-T.; Gu, Q.; Price, J.; Han, W.; Yeung, K.L. A Novel Approach to High-Performance Aliovalent-Substituted Catalysts-2D Bimetallic MOF-Derived $CeCuO_x$ Microsheets. *Small* **2019**, *15*, 1903525. [CrossRef] [PubMed]
44. Luo, M.F.; Zhong, Y.J.; Yuan, X.X.; Zheng, X.M. TPR and TPD studies of CuO/CeO_2 catalysts for low temperature CO oxidation. *Appl. Catal. A Gen.* **1997**, *162*, 121–131. [CrossRef]
45. Sumrunronnasak, S.; Chanlek, N.; Pimpha, N. Improved $CeCuO_x$ catalysts for toluene oxidation prepared by aqueous cationic surfactant precipitation method. *Mater. Chem. Phys.* **2018**, *216*, 143–152. [CrossRef]
46. Perez, A.; Molina, R.; Moreno, S. Enhanced VOC oxidation over Ce/CoMgAl mixed oxides using a reconstruction method with EDTA precursors. *Appl. Catal. A Gen.* **2014**, *477*, 109–116. [CrossRef]
47. Lu, H.; Kong, X.; Huang, H.; Zhou, Y.; Chen, Y. Cu-Mn-Ce ternary mixed-oxide catalysts for catalytic combustion of toluene. *J. Environ. Sci.* **2015**, *32*, 102–107. [CrossRef] [PubMed]
48. Zhou, G.; Lan, H.; Gao, T.; Xie, H. Influence of Ce/Cu ratio on the performance of ordered mesoporous CeCu composite oxide catalysts. *Chem. Eng. J.* **2014**, *246*, 53–63. [CrossRef]
49. Kang, R.; Wei, X.; Li, H.; Bin, F.; Zhao, R.; Hao, Q.; Dou, B. Sol-gel enhanced mesoporous Cu-Ce-Zr catalyst for toluene oxidation. *Combust. Sci. Technol.* **2018**, *190*, 878–892. [CrossRef]
50. Mo, S.; Zhang, Q.; Li, J.; Sun, Y.; Ren, Q.; Zou, S.; Zhang, Q.; Lu, J.; Fu, M.; Mo, D.; et al. Highly efficient mesoporous MnO_2 catalysts for the total toluene oxidation: Oxygen-Vacancy defect engineering and involved intermediates using in situ DRIFTS. *Appl. Catal. B Environ.* **2020**, *264*. [CrossRef]
51. Li, J.; Lu, D.-F.; Zhang, Z.; Liu, Q.; Qi, Z.-M. Hierarchical mesoporous silica film modified near infrared SPR sensor with high sensitivities to small and large molecules. *Sens. Actuators B Chem.* **2014**, *203*, 690–696. [CrossRef]
52. Zhang, Q.; Mo, S.; Li, J.; Sun, Y.; Zhang, M.; Chen, P.; Fu, M.; Wu, J.; Chen, L.; Ye, D. In situ DRIFT spectroscopy insights into the reaction mechanism of CO and toluene co-oxidation over Pt-based catalysts. *Catal. Sci. Technol.* **2019**, *9*, 4538–4551. [CrossRef]
53. Ma, L.; Seo, C.Y.; Chen, X.; Sun, K.; Schwank, J.W. Indium-doped Co_3O_4 nanorods for catalytic oxidation of CO and C_3H_6 towards diesel exhaust. *Appl. Catal. B Environ.* **2018**, *222*, 44–58. [CrossRef]
54. Abd El-Moemen, A.; Abdel-Mageed, A.M.; Bansmann, J.; Parlinska-Wojtan, M.; Behm, R.J.; Kučerová, G. Deactivation of Au/CeO_2 catalysts during CO oxidation: Influence of pretreatment and reaction conditions. *J. Catal.* **2016**, *341*, 160–179. [CrossRef]
55. Zhang, C.; Wang, C.; Huang, H.; Zeng, K.; Wang, Z.; Jia, H.-p.; Li, X. Insights into the size and structural effects of zeolitic supports on gaseous toluene oxidation over MnOx/HZSM-5 catalysts. *Appl. Surf. Sci.* **2019**, *486*, 108–120. [CrossRef]
56. Mo, S.; Zhang, Q.; Sun, Y.; Zhang, M.; Li, J.; Ren, Q.; Fu, M.; Wu, J.; Chen, L.; Ye, D. Gaseous CO and toluene co-oxidation over monolithic core–shell Co_3O_4-based hetero-structured catalysts. *J. Mater. Chem. A* **2019**, *7*, 16197–16210. [CrossRef]

57. Zhao, L.; Zhang, Z.; Li, Y.; Leng, X.; Zhang, T.; Yuan, F.; Niu, X.; Zhu, Y. Synthesis of CeaMnOx hollow microsphere with hierarchical structure and its excellent catalytic performance for toluene combustion. *Appl. Catal. B Environ.* **2019**, *245*, 502–512. [CrossRef]
58. Rainone, F.; Bulushev, D.A.; Kiwi-Minsker, L.; Renken, A. DRIFTS and transient-response study of vanadia/titania catalysts during toluene partial oxidation. *Phys. Chem. Chem. Phys.* **2003**, *5*, 4445–4449. [CrossRef]
59. Mukai, D.; Murai, Y.; Higo, T.; Tochiya, S.; Hashimoto, T.; Sugiura, Y.; Sekine, Y. In situ IR study for elucidating reaction mechanism of toluene steam reforming over Ni/La0.7Sr0.3AlO$_{3-\delta}$ catalyst. *Appl. Catal. A Gen.* **2013**, *466*, 190–197. [CrossRef]
60. Sun, H.; Liu, Z.; Chen, S.; Quan, X. The role of lattice oxygen on the activity and selectivity of the OMS-2 catalyst for the total oxidation of toluene. *Chem. Eng. J.* **2015**, *270*, 58–65. [CrossRef]
61. Besselmann, S.; Löffler, E.; Muhler, M. On the role of monomeric vanadyl species in toluene adsorption and oxidation on V2O5/TiO2 catalysts: A Raman and in situ DRIFTS study. *J. Mol. Catal. A Chem.* **2000**, *162*, 401–411. [CrossRef]